Design and Trial Production
of Microstructured ZnO Gas Sensor

Qiulin Tan[1,2,*], Chao Li[1,2,**], Wenyi Liu[1,2], Chenyang Xue[1,2],
Wendong Zhang[1,2], Jun Liu[1,2], Xiaxia Ji[1] and Jijun Xiong[1,2]

[1]Key Laboratory of Instrumentation Science & Dynamic Measurement (North University of China),
Ministry of Education, North University of China, Tai Yuan 030051, China
[2]Science and Technology on Electronic Test & Measurement Laboratory, North University of China,
Tai Yuan 030051, China

A microstructured gas sensor designed with a test electrode array is fabricated, which increases the amount of data collected by taking five groups of signals to avoid instability. By introducing a new ring heating structure, the designed sensor can effectively decrease power consumption. The relationships of surface morphology, preferred orientation and electrical properties of ZnO thin films prepared by RF magnetron sputtering with substrate temperature and annealing treatment are discussed. The results show that the resistivity of ZnO films can be as low as 6.46×10^{-3} Ω·cm under the preeminent preparation conditions of 200 °C, $\psi(Ar:O_2) = 24:3$ and working power of 180 W. By annealing for 30 min at 600 °C, the film quality improves considerably and the resistivity increases by at least three orders of magnitude. The sensor operating at 225 °C exhibits good sensitivity, and the response and recovery times for 1.0% methane and ethanol are 28 and 57 s, and 8 and 251 s, respectively. The sensor is extremely stable in 1% methane and ethanol.

1. Introduction

It is well known that gas sensors still suffer from serious shortcomings, which are mainly related to their low selectivity, low accuracy, long response time and high power consumption. The more urgent requirements for gas sensors in applications such as industrial safety and environmental pollution have been continuously driving the development of novel high-performance materials and optimial structures.[1,2] Although many studied sensor structures have been proposed, semiconductor gas sensors have hardly ever used the microstructure array to improve the data amount and a new micro-hotplate structure to reduce the power consumption.

---

*Corresponding author: e-mail: tanqiulin.99@163.com
**Corresponding author: e-mail: lichao011189@gmail.com

ZnO as a new-generation broadband semiconductor material has a hexagonal structure and a band gap of 3.37 eV at room temperature.[3] ZnO is one of the most promising materials for gas sensors owing to its large surface area, low preparation cost, high compatibility with Si microeletronic processing and high chemical stability. A large surface area is highly important for high-sensitivity gas sensors.[4–6] The surface area depends on the morphology and the ZnO nanowire with a large surface area is used for some electronics applications. ZnO is sensitive to reductive and oxidative gases, and can be used in the detection of H_2, CH_4 and liquefied petroleum gas to avoid disclosure, and in the detection of CO to control, for example, environmental pollution.[7] It was reported that the resistivity of the ZnO semiconductor changes drastically depending on the atmosphere and can decrease to 10^{-3} $\Omega\cdot$cm; thus, ZnO is an ideal conductive thin film. Therefore, the ZnO material is considered to dramatically improve the sensitivity of the gas sensors.[8,9]

ZnO films can be prepared in various ways, such as by magnetron sputtering, pulsed laser deposition,[10] chemical vapor deposition (CVD), and electron beam evaporation.[11] However, magnetron sputtering has been widely used owing to its advantages of a high deposition rate, uniformity and compactness of films and convenience for large-area preparation.[12]

In this paper, with the design of a test electrode array and a novel ring micro-hotplate structure, the fabrication of the sensor is described. Through examining and investigating the morphological characteristics, crystal orientation and resistivity of the ZnO films, the optimum sputtering parameters and annealing treatment are obtained. The sensor performance measured in methane and ethanol is discussed.

2.   Sensor Design

The sensor proposed in this paper is fabricated on the basis of a micro-hotplate with a structure array to meet the demands of practicality and feasibility. As shown in Fig. 1, the substrate material determines the n-type double parabolic silicon wafer with a crystal orientation of <100>, which grows the sacrificial layer of SiN_x on one side and the isolation layer of SiO_2 on the other side. The Ni electrode is sputtered on the isolation layer as the heating electrode. And the Ag electrode is sputtered on the Ni electrode
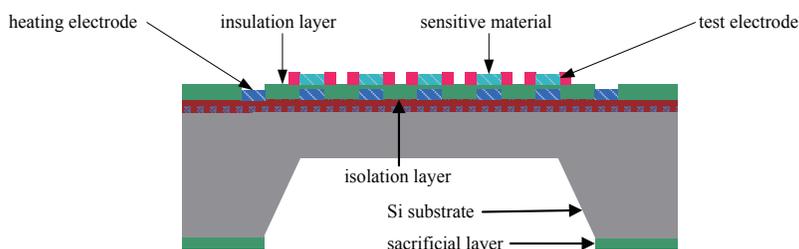
Fig. 1.   (Color online) Cross-sectional view of the gas sensor with the microstructure array.

as the test electrode. Then, a SiN$_x$ layer is designed as the insulation layer between the heating electrode and the test electrode. ZnO thin films are prepared as the gas-sensitive material by RF magnetron sputtering. Finally, to reduce the power consumption, we conduct deep silicon etching on the sacrificial layer of the gas sensor.

2.1 *Micro-hotplate design*
2.1.1 *Structure design*

In this paper, we propose a new ring heating electrode structure. Compared with the traditional serpentine heating structure, it can effectively reduce the power consumption. By simulation using the ANSYS software, the temperature distribution is shown in Fig. 2.

The thermal channel between the micro-hotplate and the external environment includes the heat conduction between dielectric films and metal wires, the heat radiation as well as the heat flux with ambient air. To simplify the modeling, we only consider the dielectric film, metal lead and conduction between top and bottom interfaces of the micro-hotplate with air in the thermal simulation of the micro-hotplate. The boundary conditions can be achieved by changing the volume heat generation rate of the heating resistor in the simulation, as the heating power of the micro-hotplate depends on the Joule heat of the heating elements. In the simulation, the heat conduction between the dielectric thin films of the micro-hotplate and the metal wires is only considered in the absolute vacuum environment; however, there is no absolute vacuum in reality, so the air convection coefficient is set to 2.5 W/m^2·K according to the literature. The heat generation rate of Ni is 2.5e^{10} W/m^3, and the thermal conductivity of SiO$_2$ is 1.4 W/m·°C. When the line widths of these two electrodes are consistent, the simulation results of the temperature distribution are as shown in Fig. 3. It is apparent that when heating the films using ring heating electrodes, the intermediate temperature of 303.4 °C is higher than
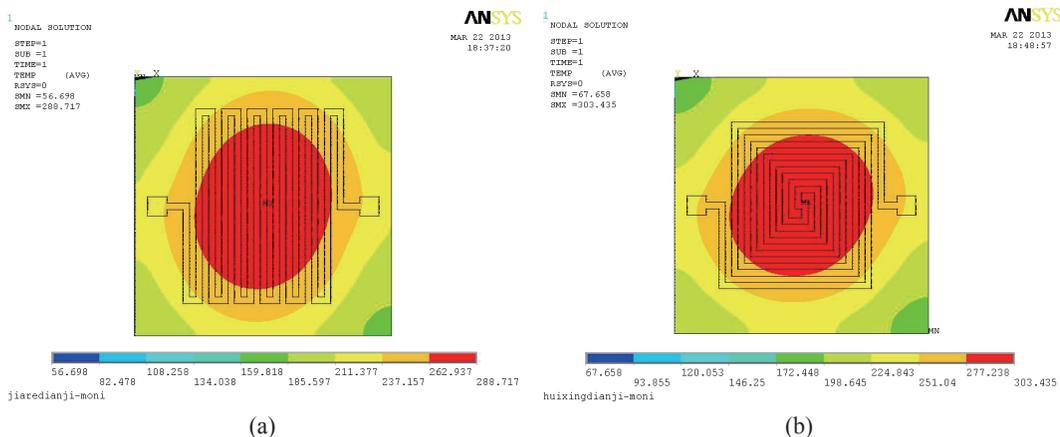
Fig. 2. (Color online) Temperature distributions of two structures: (a) serpentine heating electrode: the intermediate temperature is 288.7 °C; (b) ring heating electrode: the intermediate temperature is 303.4 °C.
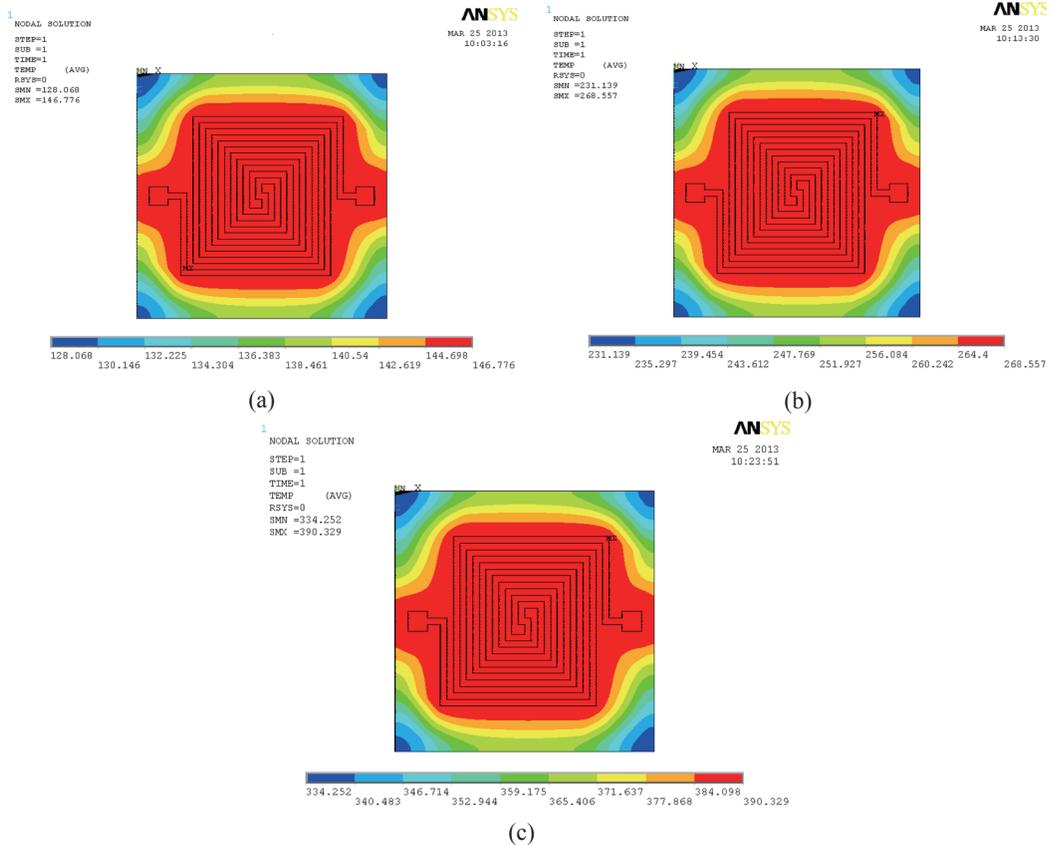
Fig. 3. (Color online) Temperature distributions of the micro-hotplate with different thickness of the heating electrode (a) 200, (b) 400, and (c) 600 nm.

that of the serpentine heating electrodes by 15 °C. Therefore, in the case of a consistent operating temperature, using a traditional serpentine heating electrode more effectively reduces the power consumption.

2.1.2 *Thickness design*

The factor that affects the thermal field distribution, such as the thickness of a heating electrode, is analyzed using ANSYS. The heating electrode thicknesses are 200, 400, and 600 nm. In the simulation, the substrate thickness is 200 μm, and the thicknesses of the isolation and insulation layers are 500 and 800 nm, respectively; the results are shown in Fig. 3.

From Fig. 3, the heating electrode thickness does not affect the gradient distribution of the micro-hotplate temperature; it only changes the overall temperature of the heating device. Therefore, the heating device sizes, required temperature and substrate thickness are the factors that affect the thickness of a heating electrode.

2.2 *Isolation layer design*

We simulate the effect of varying insulation layer thickness on the thermal field distribution. The thicknesses are 100, 300, and 500 nm. It is found that the SiO_2 isolation layer thickness is irrelevant to the micro-hotplate temperature. The maximum temperature change of the micro-hotplate in the central region is only about 3 °C when the SiO_2 isolation layer thickness varies from 100 to 500 nm (Fig. 4), which is mainly because the SiO_2 thickness is much smaller than the substrate thickness. Here, we consider 500 nm as the SiO_2 isolation layer thickness.

2.3 *Test electrode design*

In comparison with the interdigital electrode, the designed test electrode can increase the amount of data collected by taking five groups of signals to avoid instability, which is due to a single signal that generates a signal drift [Fig. 5(f)].
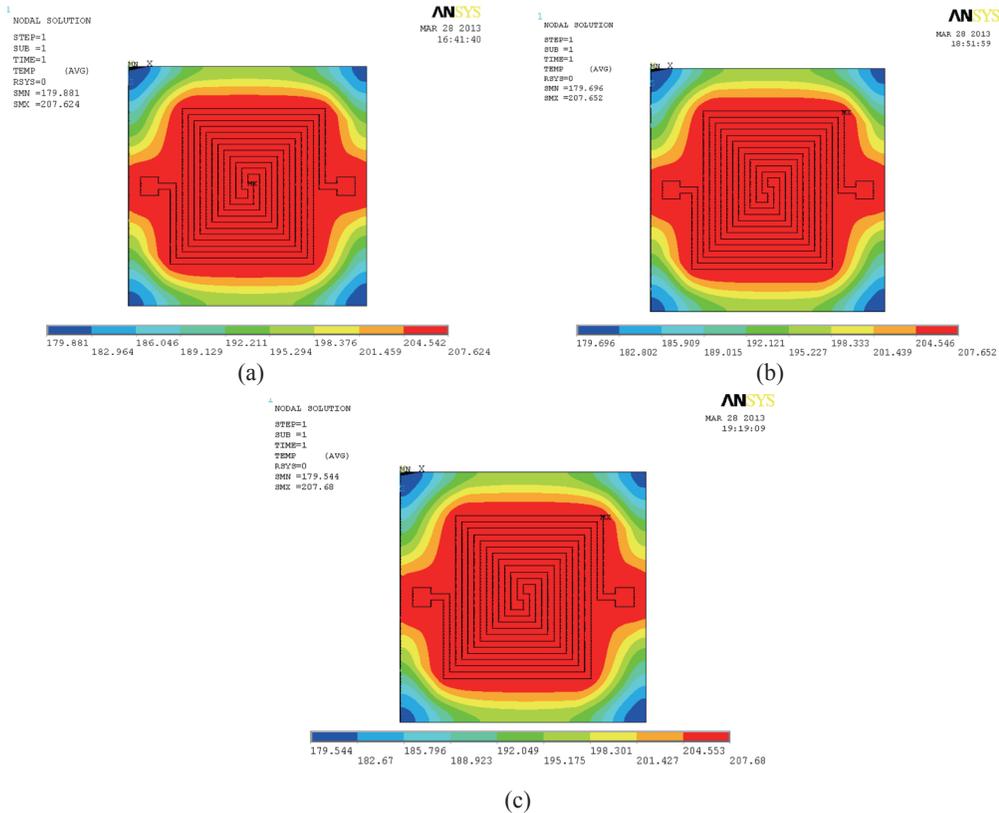
Fig. 4.   (Color online) Temperature distributions of the micro-hotplate with different isolation layer thicknesses: (a) 100, (b) 300, and (c) 500 nm.
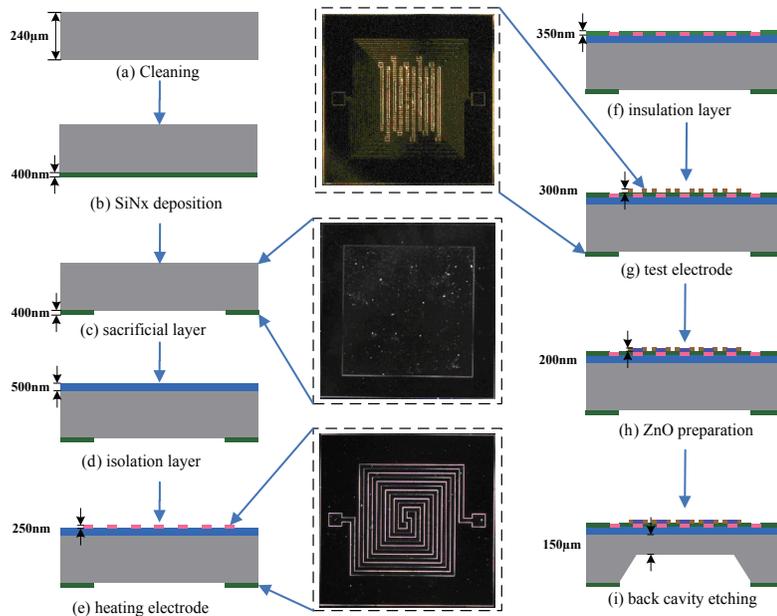
Fig. 5.   (Color online) Major fabrication steps.

3.   Sensor Preparation

The designed sensor is fabricated by silicon micromachining; the detailed preparation steps are as shown in Fig. 5.

(a) The Si wafer is cleaned with acetone, isopropyl alcohol and deionized water using an ultrasonic cleaner in turn.

(b) The 400 nm Si_3N_4 layer is deposited using an ICP-CVD 100 device with 40 sccm gas ventilation for 15 min.

(c) The sacrificial layer is prepared by photolithography and RIE etching, similarly to the protective layer with back cavity etching [Fig. 5(c)].

(d) The SiO_2 layer is also prepared by the ICP-CVD method as the isolation layer, and the growth rate is approximately 37 nm/min. The prepared thickness is 500 nm.

(e) By photolithography to form the heating electrode pattern, Ti is sputtered to 50 nm to enhance the adhesion with the substrate and Ni is sputtered to 200 nm as the electrode material. Finally, the heating electrode is achieved using lift-off technology [Fig. 5(e)].

(f) Considering the signal interference, the insulation layer is prepared between the heating electrode and the test electrode. Here, we consider 350 nm as the insulation layer thickness.

(g) The procedure is the same as in (d), except that the test electrode material is 50 nm Ni/ 250 nm Ag [Fig. 5(f)].

(h) ZnO thin films are prepared by RF magnetron sputtering; the specific parameters are illustrated in § 4.1.

(i) Two methods, namely, wet etching and deep silicon etching, can be chosen in the final fabrication process. However, in the deep silicon etching, two electrode structural layers raised on another sensor surface may be damaged. Thus, wet etching is selected in the final fabrication process. With 40% KOH at 80 °C, the corrosion rate of silicon reaches 0.934 μm/min.

4. Experiment on ZnO thin films

4.1 *Preparation of ZnO thin films*

ZnO thin films are prepared on Si substrates by RF magnetron sputtering using Lab18 of the Suzhou Institute of Nano-Tech and Nano-Bionics (SINANO), Chinese Academy of Sciences. In the processing, we use a Zn (99.99%) target. When the vacuum system is pumped to 8.0×10^{-6} Pa and the substrate reaches the desired temperature, Ar and O_2 are introduced into the chamber as the sputtering gases. ZnO thin films are prepared with different sputtering parameters such as temperature, power, oxygen-argon ratio and annealing temperature. In this paper, the relationships of the surface morphology, preferred orientation and resistance of ZnO thin films with these deposition parameters are discussed. Moreover, we also obtain the optimum preparation parameter, as shown in Table 1. The growth rate of ZnO thin films is 6 nm/min under this condition.

4.2 *Structural characterization*

The film thickness is measured using a step instrument (Veeco, DEKTAK 150). The crystal structure is characterized by X-ray diffraction with a Bruker AXS X'pert diffractometer with a Kα line ($\lambda = 0.154056$ nm). The surface morphology is observed by atomic force microscopy (Dimension 3100). The resistance characteristic is measured using a CRESBOX four-point probe.

4.2.1 *Substrate temperature characterization*

ZnO films grown on the Si substrate exhibit a peak located near 34.4° and a peak at around 62.8°. According to the Joint Committee on Powder Diffraction Standards (JCPDS) card (No. 36-1451), the peaks corresponds to ZnO (002) and ZnO (103). As the substrate temperature increases, the (002) peak intensity increases. Except for the (002) peak, ZnO thin films prepared at normal temperature exhibit a (103) peak. This indicates that the preferred orientation deteriorates and shows a polycrystalline state. FWHMs are

Table 1
Preparation parameters of ZnO thin films.

Preparation parameter	Value
Target-substrate distance (cm)	15
Oxygen-argon ratio [Ψ(Ar:O_2)]	24:3
Substrate temperature (°C)	200
RF power (W)	180
Annealing atmosphere	O_2 ($\geq$99.99%)
Annealing temperature (°C)	600
Annealing time (min)	30

0.337 and 0.281°. The crystallite size is calculated using the Scherer formula [eq. (1)],[13] which is expressed as

$$D = 0.94\lambda/B\cos\theta, \tag{1}$$

where D is the grain size, λ is the wavelength of the X-ray, B is the FWHM of the diffraction peak, and θ is the diffraction angle corresponding to the diffraction peak. The grain sizes are 25.7 and 30.1 nm, which clearly show that the increasing substrate temperature is conducive to the growth of the films. This is consistent with the conclusions drawn concerning the surface morphology of ZnO thin films, as shown in Fig. 6. The surface roughnesses (RMS) of the thin films are 7.53 and 3.77 nm. It is observed that the thin film surface becomes smoother and more uniform, and the crystalline quality significantly improves with increasing sputtering temperature.

As a consequence, the substrate temperature has an enormous effect on the crystalline growth of ZnO thin films. This is because at lower temperatures, the sputtered zinc and oxygen atoms with lower energies pass into the lattice position before reaching the position of the lowest energy; hence, the orientation of the ZnO thin films deteriorates.[14] When the substrate temperature is increased, the activity of the oxygen atoms is enhanced, which is conducive to filling the oxygen vacancies; thus, the crystalline quality is markedly improved.

(a)

(b)
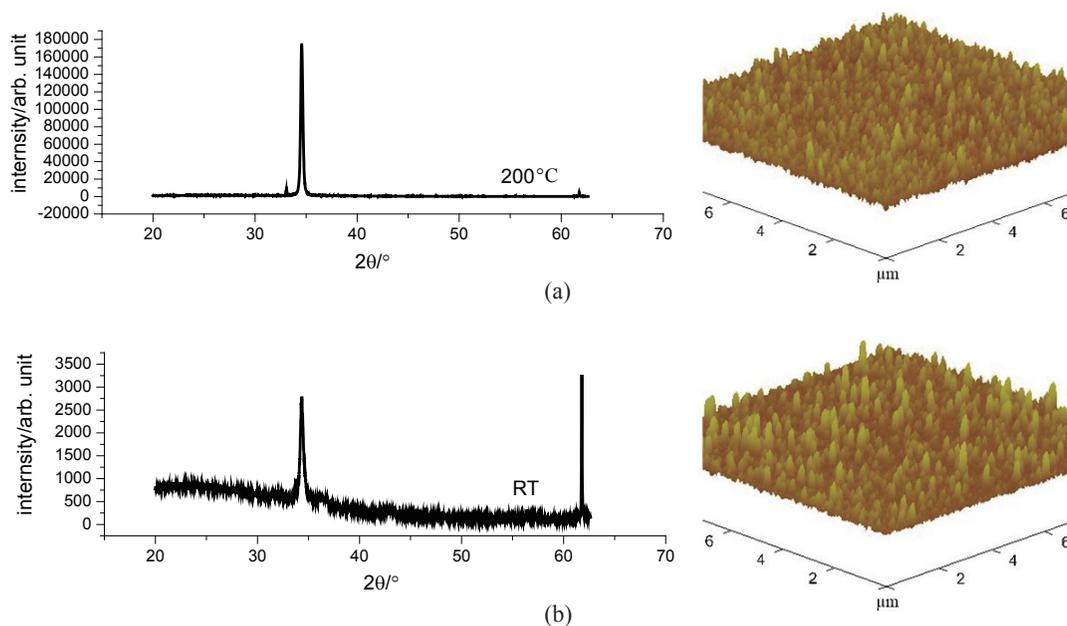
Fig. 6. (Color online) XRD patterns and three-dimensional surface morphologies of ZnO thin films prepared with different substrate temperatures (a) RT and (b) 200 °C.

4.2.2 *Annealing temperature characterization*

After the preparation of ZnO thin films, the films usually need to be annealed for optimization to further reduce the defect density and enhance the properties. In this paper, ZnO thin films prepared at the substrate temperature are annealed for 30 min at 400, 600, and 800 °C in air atmosphere. With increased annealing temperature, the (002) peak intensity increases at the beginning and decreases after it reaches a maximum value at the annealing temperature of 600 °C, as shown in Fig. 7(a). It is verified that 600 °C is most suitable for the preferred orientation growth of the films. However, the results also indicate that the effects of annealing on the structure and orientation of ZnO thin films are minimal, because there are no other diffraction peaks except the (002) diffraction peak.

The full widths at half maximum (FWHW) are 0.305, 0.245, 0.24, and 0.265° for the corresponding ZnO thin films. The grain size of the thin films is calculated, as shown in Fig. 7(b). It can be seen that when the annealing temperature increases, the grain size gradually increases at the beginning and diminishes after 600 °C. Further increase in annealing temperature to 800 °C leads to reductions in (002) peak intensity and grain size. A high annealing temperature damages the surface, resulting in the deterioration of the crystallite growth process. Consequently, the optimal annealing temperature of ZnO thin films is 600 °C, which is verified from the surface images of ZnO thin films, shown in Fig. 8. It is well known that the annealing process can increase the oxygen content of the thin films. Thus, the oxygen vacancies and defects (*e.g.*, interstitial zinc atoms) can obtain sufficient diffusion activation energy to be eliminated gradually. As a result, the grains will be merged gradually and become larger; thus, the thin films tend to be more compact. However, exorbitant annealing temperatures have a disadvantageous effect on the disappearance of oxygen vacancies, which makes it difficult to obtain a large grain structure.
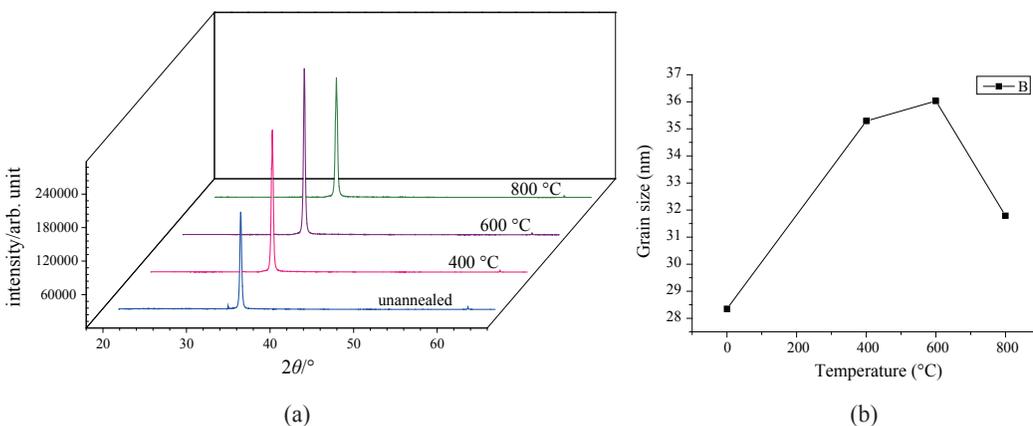
Fig. 7. (Color online) XRD and FWHM patterns of ZnO films under different annealing temperatures.
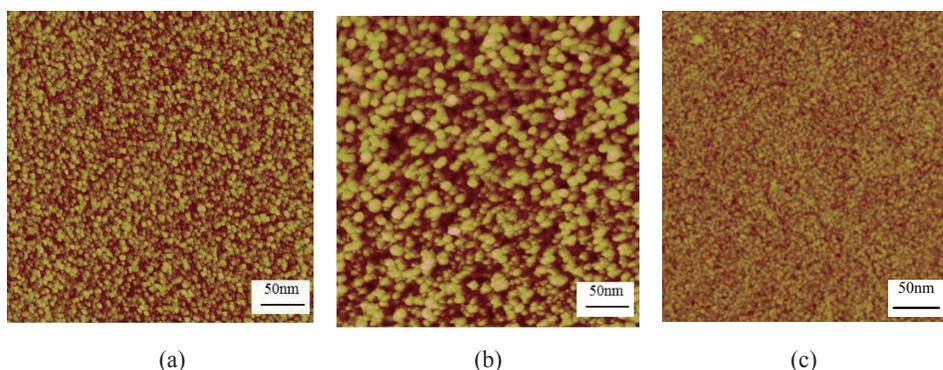
Fig. 8.   (Color online) Surface topography images of ZnO thin films under different annealing temperatures: (a) 400, (b) 600, and (c) 800 °C.

4.3   *Characterization of electrical properties*

The sample films are prepared with the above parameter (§ 4.1) under different argon-oxygen ratios. The resistivity results are shown in Table 2, which indicates that with increasing argon-oxygen ratio, the resistivity of ZnO thin films decreases and reaches 6.46×10^{-3} $\Omega \cdot$cm at $\psi(Ar:O_2) = 24:3$. It is considered that much of Zn is ionized into Zn^{2+} and Zn ions are chemically active during the sputtering process. After annealing, the resistivity of the films changed dramatically and improved by at least three orders of magnitude, which is attributed to the chemical adsorption of oxygen on the surface under annealing treatment in air. Moreover, ZnO thin films annealed at 600 °C have a higher resistivity, which will establish the condition for ZnO thin films as the sensitive material of gas sensors.

5.   Results and Discussion

The sensors respond to the variations in gas concentration and operating temperature, which are usually induced by oxygen adsorption on the ZnO thin films. When exposed to air, the resistance of ZnO thin films will change dramatically. In order to obtain the optimal operating temperature, the changes in the resistance of the sensors are measured. The response sensitivity S is calculated using the formula

$$S = (R_a - R_g) / R_a, \tag{2}$$

where R_g is the sensor resistance in the test gas and R_a is the sensor resistance in air.

As revealed by Fig. 9(a), the maximum response for gas concentrations is acquired at around 225 °C. Figure 9(b) shows that the sensor exhibits fairly good response (CH_4, 75–84% at 0.01–1.0%; CH_3CH_2OH, 70–87% at 0.01–1.0%) at 225 °C. Compared with ref. 15, the optimal operating temperature for methane sensing is lowered from 250 to 225 °C.

Figure 10 shows the variations in response time and recovery time versus gas concentration. With the maximum response of 84% at the CH_4 concentration of 1.0%,

Table 2
Resistivity and sheet resistance of ZnO thin films.

Sample	Unannealed		Annealed at 400 °C		Annealed at 600 °C	
	Resistivity ($\Omega \cdot$cm)	Sheet resistance (Ω/sq)	Resistivity ($\Omega \cdot$cm)	Sheet resistance (Ω/sq)	Resistivity ($\Omega \cdot$cm)	Sheet resistance (Ω/sq)
1 [ψ(Ar:O$_2$) = 4:1]	–	–	–	–	–	–
2 [ψ(Ar:O$_2$) = 6:1]	–	–	270.6	7.52	314.1	10.56
3 [ψ(Ar:O$_2$) = 7:1]	7.15×10^{-2}	1.6×10^3	116.2	10.6×10^{-3}	251.3	123×10^3
4 [ψ(Ar:O$_2$) = 8:1]	6.46×10^{-3}	143.7	15.91	1.39×10^{-3}	62.75	283×10^3
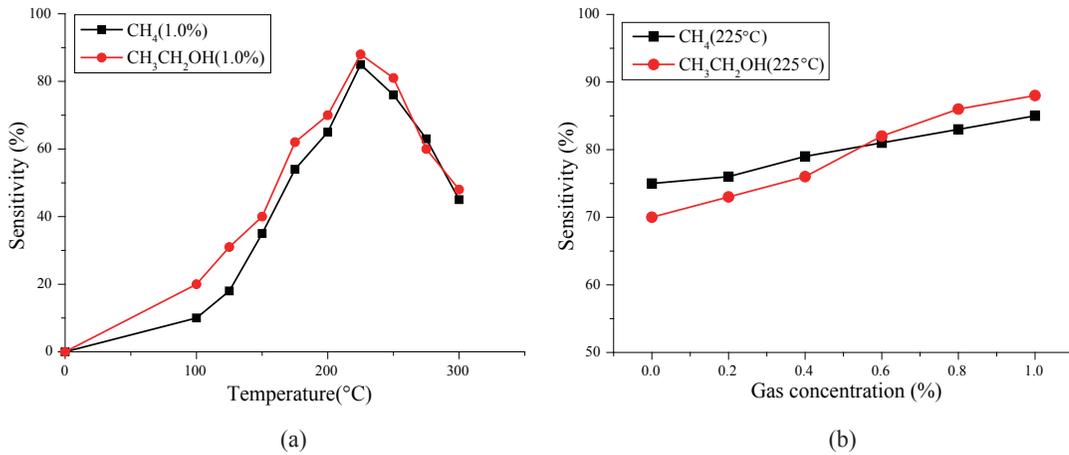
Fig. 9.   (Color online) (a) Response sensitivity as a function of temperature for different gases; (b) Response sensitivity as a function of gas concentration for different gases at 225 °C.
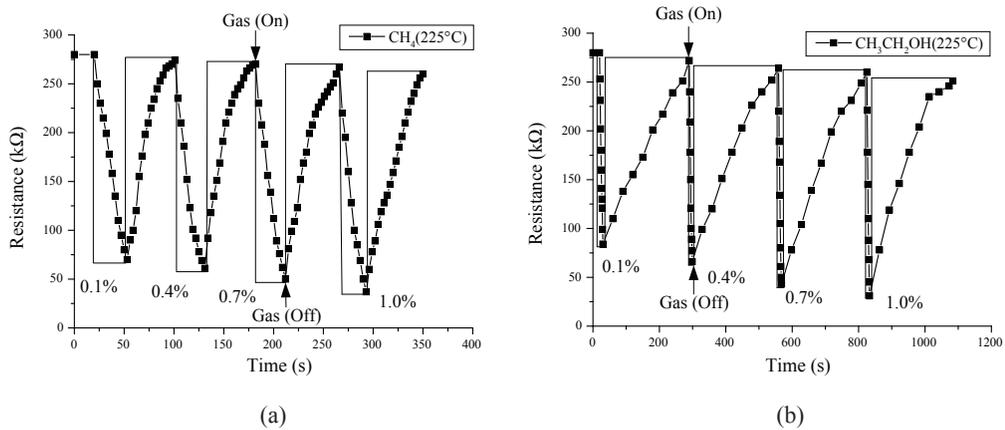
Fig. 10. Transient response characteristic at 225 °C for different gas concentrations: (a) CH$_4$ and (b) CH$_3$CH$_2$OH.
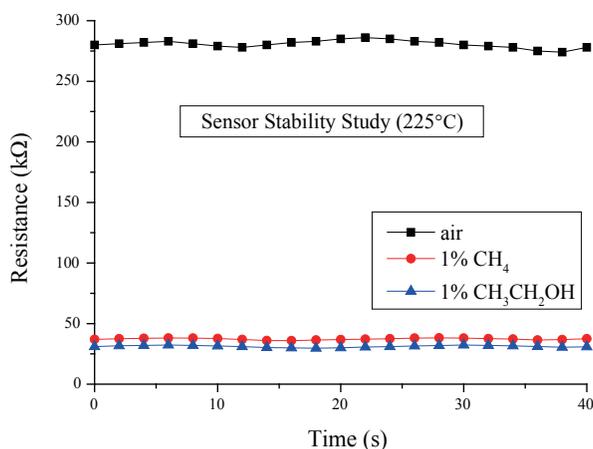
Fig. 11. (Color online) Stability study of the sensor with air, 1.0% CH_4 and CH_3CH_2OH at 225 °C.

the corresponding response and recovery time are 28 and 57 s, respectively. On the other hand, the corresponding response and recovery time are 8 and 251 s with the maximum response of 87% at the CH_3CH_2OH concentration of 1.0%.

The study of the sensor stability is carried out with air, 1.0% CH_4 and CH_3CH_2OH for 5 days (at an average of 8 h per day) and the results are shown in Fig. 11. It can be seen that the sensor exhibits sufficient stability with negligible resistance variation. The variations in resistance are only ±2% in air, ±3% in 1.0% CH_4, and ±4% in 1.0% CH_3CH_2OH.

6.   Conclusions

In this work, gas sensors based on ZnO thin films, which have an advantage over traditional sensors for improving the heating temperature and the accuracy of detection, are designed and fabricated. Here, we propose a new ring structure of a micro-hotplate and the microstructure array of the test electrode. Furthermore, the most suitable sputtering condition of ZnO thin films can be obtained. With the sputtering conditions of 200 °C, $\psi(Ar:O_2)$ = 24:3 and 180 W, the lowest resistivity of 6.46×10^{-3} Ω·cm can be obtained. The crystalline quality and crystalline structure need to be optimized considerably at the annealing temperature of 600 °C for 30 min in air. The sensor operating at 225 °C exhibits good sensitivity, response and recovery time for methane and ethanol (0.1–1.0%). The sensor stability in 1% methane and ethanol is also excellent. In future works, filterable thin films are expected to be prepared on sensing films to improve the sensor selectivity.

Acknowledgements

References

1　A. Vergara, E. Llobet, J. Brezmes, P. Ivanov, C. Cane and I. Gracia: Sens. Actuators, B **123** (2007) 1002.
2　B. J. Kim and J. S. Kim: Mater. Chem. Phys. **138** (2013) 366.
3　C. M. Firdaus, M. S. B. Shah Rizam, M. Rusop and S. Rahmatul Hidayah: Procedia Eng. **41** (2012) 1367.
4　M. S. Kima, K. G. Yima and H. Y. Choi: J. Cryst. Growth **326** (2011) 195.
5　H. Gleiter: Prog. Mater. Sci. **33** (1989) 223.
6　S. L. Bai, L. Y. Chen, R. X. Luo, K. W. Zhang, D. Q. Li, A. F. Chen and C. C. Liu: IEEE Sens. J. **11** (2011) 1969.
7　G. S. Trivikrama Rao and D. Tarakarama Rao: Sens. Actuators, B **55** (1999) 166.
8　S. H. Wei, Y. Yu and M. H. Zhou: Mater. Lett. **64** (2010) 2284.
9　H. Ishizaki, M. Imaizumi, S. Matsuda, M. Izaki and T. Ito: Thin Solid Films **411** (2002) 65.
10　V. Cracium, J. Elders, and J. G. E. Gardeniers: Appl. Phys. Lett. **65** (1994) 2963.
11　A. Kuroyanagi: Jpn. J. Appl. Phys. **28** (1989) 219.
12　A. M. Rosa, E. P. da Silva, M. Chaves, L. D. Trino, P. N. Lisboa-Filho, T. F. da Silva, S. F. Durrant and J. R. R. Bortoleto: J. Mater. Sci.: Mater. Electron. **24** (2013) 3143.
13　D. M. Smilgies: J. Appl. Cryst. **42** (2009) 1030.
14　Y. Zhou, M. D. Qiu, Q.X. Zhao, X. H. Li, Y. C. Peng and B. T. Liu: J. Funct. Mater. **40** (2009) 735.
15　P. Bhattacharyya, P. K. Basu, B. Mondal and H. Saha: Microelectron. Reliab. **48** (2008) 1772.